Research Square

Preprints are preliminary reports that have not undergone peer review.
They should not be considered conclusive, used to inform clinical practice,
or referenced by the media as validated information.

Physics-Constrained Deep Sequential Learning for Continuous Pore Pressure and Fracture Gradient Prediction in Heterogeneous Carbonate Reservoirs Using Conventional Wireline Logs

zainulabdeen HASAN

salahhasan@graduate.utm.my

University of Technology Malaysia

mohd ZAIDI JAFFAR

University of Technology Malaysia

Amni haslinda alpandi

University of Technology Malaysia

ahmed alameeny

University of Baghdad

Research Article

Keywords: Pore pressure prediction, Fracture gradient, Carbonate reservoirs, Deep sequential learning, Physics-informed neural networks, Bidirectional GRU, Wellbore stability, Conventional wireline logs

Posted Date: November 12th, 2026

DOI: https://doi.org/10.21203/rs.3.rs-11414991/v1

License: This work is licensed under a Creative Commons Attribution 4.0 International License.
Read Full License

Additional Declarations: No competing interests reported.

Physics-Constrained Deep Sequential Learning for Continuous Pore Pressure and Fracture Gradient Prediction in Heterogeneous Carbonate Reservoirs Using Conventional Wireline Logs

- **[Zainulabdeen salah Hasan, Mohd Zaidi Jaffar, Amni Haslinda Alpandi, Sharul Nizam] a*,[A. Alameen] b**

[a] Department of Petroleum Engineering, [University of Technology Malaysia], Johor, Malaysia

[b] Department of Petroleum Engineering, [University of Baghdad], Baghdad, Iraq

** Corresponding author e-mail: [salahhasan@graduate.utm.my]*

Abstract

Accurate assessment of predrilling and post-drill of formation pore pressure (Pp) and fracture gradient (FG) is quite important for defining a safe mud-weight window and avoiding kicks. Also, it is crucial for mitigating lost circulation and improving casing shoe depths. In Middle Eastern reservoirs, specifically heterogeneous carbonate reservoirs, traditional empirical correlations such as Eaton's sonic and resistivity equations as well as Bowers' velocity-stress relations and Matthews-Kelly fracture models often fail. Failure is attributed to carbonate rock stiffness, diagenetic cementation and secondary porosity beside chemical compaction decouple acoustic velocity from vertical effective stress ($\sigma'v$). Moreover, particular dipole sonic logs (Δts), borehole image logs and laboratory rock-mechanics core measurements are not often acquired across entire development wells because of extreme cost and operational hazards. However, using conventional wireline logs and as follow; Gamma Ray (GR); Bulk Density (ρb); Neutron Porosity (ϕN); Deep Resistivity (Rt); Caliper (CALI), and Compressional Sonic transit time (Δtc) is to overcome these limitations. This study suggests a novel work of Physics-Constrained Bidirectional Gated Recurrent Unit with Temporal Depth Attention (PC-BiGRU-Attn) framework. When well-log profiles are formulated as bidirectional stratigraphic depth sequences (L=31, samples=1.94 m aperture) instead of isolated depth points, the sequential network captures vertical compaction transitions beside caprock sealing effects and lithofacies boundaries across carbonate subunits. Both, Terzaghi's effective stress principle and geomechanical boundary constraints ($Phyd \leq Pp < Pf \leq \sigma v$) are embedded directly into a hybrid physics-informed loss function to eradicate physically excluded pressure spikes in uncalibrated intervals. Field validation across three anonymized wells (WELL X1, WELL X2, and WELL X3, comprising 60,186 depth measurements spanning 1,247.12–3,392.62 m) demonstrates that the proposed PC-BiGRU-Attn architecture outperforms standalone empirical methods (Eaton, Bowers, and Matthews–Kelly), Multilayer Perceptrons (MLP), Gradient Boosted Trees (GBR), 1D Convolutional Neural Networks (1D-CNN), and standard Bidirectional Long Short-Term Memory (Bi-LSTM) networks. On the unseen blind test well (WELL X2, N = 8,946), PC-BiGRU-Attn achieves a coefficient of determination (R^2) of 0.9876 (RMSE = 60.14 psi, MAPE = 1.30%) for pore pressure and $R^2 = 0.9961$ (RMSE = 32.39 psi, or FG RMSE = 0.0047 psi/ft, MAPE = 0.46%) for fracture pressure, reducing blind-well pore

and fracture pressure RMSE by 37.2% and 49.6%, respectively, relative to point-wise ANN models while maintaining a 0.00% physical violation rate.

Keywords: Pore pressure prediction; Fracture gradient; Carbonate reservoirs; Deep sequential learning; Physics-informed neural networks; Bidirectional GRU; Wellbore stability; Conventional wireline logs.

1. Introduction

When a drilling program wants to be designed in a safe and economical manner in deep hydrocarbon basins, it requires continuous and high-resolution profiles of formation pore pressure and fracture pressure, or fracture gradient FG=Pf/z, along the entire wellbore trajectory [1, 3]. Through drilling actions, the wellbore pressure applied by the drilling fluid column quantified by the static Mud Weight (MW) and dynamic Equivalent Circulating Density (ECD), must be kept strictly within the safe operational drilling window [4, 5]. The lower bound of the window is administered by the formation pore pressure gradient (Pp/z) and the wellbore shear collapse pressure whereas the upper bound is dictated by the formation fracture gradient. If the wellbore fluid pressure decreases below Pp, formation fluids (eg; oil, gas, or brine) influx into the borehole, which will activate well kicks or catastrophic blowouts [6]. Contrariwise, if the ECD exceeds FG, hydraulic tensile failure occurs in the borehole wall, resulting in severe lost circulation, formation damage, and costly Non-Productive Time (NPT) [7, 12].

Historically, log-based pore pressure and fracture gradient prediction has been dominated by classical effective-stress and normal-compaction correlations developed by Terzaghi and Biot [8], Hottman and Johnson [9], Hubbert and Willis [10], Matthews and Kelly [11], Eaton [12, 13], Daines [14], and Bowers [15]. While such empirical models succeed in young, clay-dominated siliciclastic basins, they break down severely in Middle Eastern carbonate reservoirs—which host over 60% of conventional oil reserves across Iraq, Iran, and the Arabian Gulf (including the Hartha, Sadi, Tanuma, Khasib, Mishrif, Yamama, Shuaiba, Asmari, and Jeribe formations) [16–22]—due to three fundamental petrophysical challenges:

1. Breakdown of Mechanical Compaction Trends (NCT): Carbonate sediments undergo rapid early marine cementation, dissolution, dolomitization, and chemical compaction (stylolitization). Porosity and sonic transit time (Δtc) are governed by diagenetic fabric rather than vertical effective stress ($\sigma'v$) alone, making NCT placement highly subjective [1, 4, 17].

2. High Matrix Stiffness and Secondary Porosity Anomalies: Calcite (Km ≈ 70–76 GPa) and dolomite (Km ≈ 90–95 GPa) host rigid secondary vugs, molds, and fractures [21]. High-stiffness vuggy limestones exhibit fast acoustic velocities (low Δtc) despite hosting overpressure, causing Eaton's sonic equation to severely underestimate Pp by up to 1,150 psi [4, 17].

3. Scarcity of Dipole Shear Sonic (Δts) and Core Data: Classical fracture gradient models require Poisson's ratio (ν) and Biot's coefficient (α), which depend on shear wave slowness (Δts) and core tests [12, 14]. In most legacy and development wells (WELL X1 and WELL X2), only

conventional logs exist, and in deep offset wells (WELL X3), even compressional sonic logs may be missing.

2. Comprehensive Literature Review

2.1 Classical Effective-Stress and Empirical Pore-Pressure Formulations

Subsurface geopressure analysis is grounded in Terzaghi and Biot's poroelastic effective stress principle ($\sigma'v = \sigma v - \alpha$ Pp) [1, 8]. Hottman and Johnson (1965) [9] recognised that shale porosity and acoustic transit time decline logarithmically with burial depth along a Normal Compaction Trendline (NCT). While Eaton (1975) [13] formulated power-law empirical equations involving abnormal pore pressure to normal-to-observed sonic transit-time ratios, $(\Delta tn/\Delta tc)^{3.0}$, and resistivity ratios, $(Rt/Rn)^{1.2}$. Furthermore, Bowers (1995) [15] later presented virgin compaction (parameters A, B) and power-law unloading (exponent U) velocity–effective stress relations to capture fluid expansion and thermal cracking. In addition, Zhang (2011, 2013) [1, 2] modified Eaton's technique using depth-dependent exponential NCT curves bounded by both mudline transit time (Δtml) and mineral matrix transit time (Δtm).

2.2 Evolution of Fracture Gradient and Borehole Breakdown Models

Hubbert and Willis (1957) [10] demonstrated that hydraulic fractures propagate perpendicular to the minimum principal stress (σh), establishing theoretical bounds between 1/3 and 1/2 of effective overburden stress. Matthews and Kelly (1967) [11] introduced an empirical matrix stress coefficient (Ki), while Eaton (1969) [12] derived the uniaxial-strain poroelastic relation $K0 = \nu / (1 - \nu)$. Daines (1982) [14] superimposed a tectonic stress component (σt) onto Eaton's equation to account for compressional tectonic regimes [7, 22].

2.3 Geomechanical Complexities in Iraqi and Middle Eastern Carbonate Reservoirs

Recent studies across Iraqi carbonate fields underscore the limitations of standalone empirical correlations. In the Tanuma Formation, Al-kinani et al. (2022) [17] documented a 1,550 psi divergence between Eaton (4,650 psi) and Bowers (3,100 psi). In the Mishrif Formation of the Buzurgan oilfield, Al-Shammari et al. (2023) [18] identified severe overpressure anomalies across six wells (up to 5,705 psi at 4,020 m in units MA, MB21, MC1, and MC2). In the Asmari Formation, Al Said Naji et al. (2023) [4] calibrated log predictions with MDT data (6,328–7,538 psi) across three wells, proving that Eaton's fixed 80 µs/ft baseline failed to isolate overpressured zones whereas Bowers' method achieved <3.0% error. Similar facies-driven NCT shifts were confirmed by Tawfeeq et al. (2024) [19] in northeastern Iraq and Al-Jaberi et al. (2025) [22] in the Rumaila field.

2.4 Deep Sequential Networks and Physics-Informed Approaches

Data-driven machine learning models, including BPNN, GRNN and GMDH polynomial networks as well as feedforward ANNs, across 305 Middle Eastern wells R^2=0.974 for Pp and 0.998 for FG; also, 385 southern Iraqi wells have improved nonlinear regression but process each

depth point self-sufficiently [3, 6, 23, 25, 26]. Sequential architectures such as hybrid LSTM-BP, adjacent-well MAE = 2.34 MPa, and stacking ensembles (R^2=0.895–0.936) capture depth trends but lack explicit poroelastic constraints in their loss functions [27-29]. Table 1 presents these representative studies.

Table 1: Comparative synthesis of classical empirical, Middle Eastern carbonate, and AI/ML studies for pore pressure (Pp) and fracture gradient (FG) prediction.

Study / Reference	Target	Lithology / Basin	Methodological Approach	Key Findings & Carbonate Limitations
Hubbert & Willis (1957) [10]	FG	Sedimentary	Theoretical min. stress (σh ≈ 1/3–1/2 σ'v + Pp)	Fixed stress ratio ignores lithology Poisson's ratio shifts.
Hottman & Johnson (1965) [9]	Pp	Gulf Coast Shale	Semi-log shale Δt and Rt departure from NCT	Valid only in monotonous plastic clays under undercompaction.
Matthews & Kelly (1967) [11]	FG	Clastic	Empirical matrix stress coefficient (Ki)	Neglects elastic stiffness contrasts in carbonate–evaporite beds.
Eaton (1969, 1975) [12, 13]	Pp, FG	Shale / Clastic	Power-law NCT ratios (Δtn/Δtc)^3.0 and v(z)	Fails in cemented/vuggy carbonates and unloading zones.
Daines (1982) [14]	FG	Wildcat Mixed	Tectonic stress (σt) + Eaton uniaxial stress	Requires continuous Poisson's ratio and LOT calibration.
Bowers (1995) [15]	Pp	Mixed / Shale	Virgin (A, B) & unloading (U) velocity–stress	Captures fluid expansion; requires local parameter tuning.
Zhang (2011, 2013) [1, 2]	Pp, FG	Sedimentary	Exponential depth-dependent NCT Δtn(z)	Improves NCT fit, but carbonate diagenesis shifts baseline.
Ghaedi et al. (2021) [16]	Pp, Vs	Carbonate (Iran)	Terzaghi/Biot (α=0.7) & Castagna Vp–Vs	Confirmed coupling between Vp/Vs, ν, and carbonate Pp.

Study / Reference	Target	Lithology / Basin	Methodological Approach	Key Findings & Carbonate Limitations
Li et al. (2022) [27]	Pp	Clastic / Mixed	Hybrid sequential LSTM-BP (18 inputs)	Adjacent-well MAE = 2.34 MPa; beat SVM and BPNN.
Abdelaal et al. (2022) [3]	Pp, FG	Middle East (305 wells)	Feedforward ANN on 2,820 mixed datasets	R^2 = 0.974 (Pp), 0.998 (FG); point-wise without sequence memory.
Al-Shammari et al. (2023) [18]	Pp, FG	Mishrif Carb. (Iraq)	Log-based Eaton evaluation across 6 wells	Identified overpressure up to 5,705 psi at 4,020 m in Buzurgan.
Al Said Naji et al. (2023) [4]	Pp, σv	Asmari Carb. (Iraq)	Eaton slowness vs. Bowers calibrated with MDT	Eaton 80 µs/ft baseline failed; Bowers achieved <3% error.
Tawfeeq et al. (2024) [19]	Pp, FG	Tertiary Carb. (Iraq)	Sonic NCTL & Eaton FG across 3 wells	Showed strong sensitivity of NCTL to lateral facies variations.
Wang et al. (2025) [28]	Pp	Offset Wells	Stacking ensemble (BPNN, CNN, LSTM, LightGBM)	Blind R^2 = 0.895–0.936; unconstrained MSE loss function.
Present Study (WELL X1–X3)	**Pp, FG**	**Carbonate (Iraq)**	**Physics-Constrained Bi-GRU + Attention (PC-BiGRU-Attn)**	**Blind R^2 = 0.9876 (Pp) & 0.9961 (Pf); 0.00% physical violations.**

3. Geological Setting and Wireline Dataset Description

The dataset analyzed in this study comprises 60,186 conditioned high-resolution wireline log measurements (sampling interval Δz = 0.0625 m) acquired across three vertical wells—anonymized as WELL X1 (N = 20,938; 1,247.12–2,555.75 m), WELL X2 (N = 8,946; 1,780.00–2,339.12 m), and WELL X3 (N = 30,302; 1,498.62–3,392.62 m)—penetrating a Cretaceous–Tertiary carbonate reservoir succession in the Central Mesopotamian Basin of Iraq [4, 18–20]. The stratigraphic section is subdivided into four geomechanical units: Unit A (1,247–1,780 m, Upper Caprock and Marl Seal), Unit B (1,780–2,150 m, Upper Bioclastic Carbonate Pay), Unit C (2,150–2,556 m, Main Vuggy and Moldic Carbonate Pay hosting four electrofacies), and Unit D (2,556–

3,393 m, Deep Tight Dolomitic Carbonate Succession penetrated by WELL X3). Table 2 summarizes the statistical distribution of all conditioned curves across the three wells.

Table 2: Statistical summary of conditioned wireline logs and reference pressure parameters across WELL X1, WELL X2, and WELL X3 (N = 60,186 samples).

Parameter	Symbol (Unit)	Min	Max	Mean	Std. Dev.	Skewness	Primary Geomechanical Role
True Vertical Depth	z (m)	1247.13	3392.62	2198.96	518.01	0.457	Gravitational load & NCT baseline
Gamma Ray	GR (gAPI)	2.83	115.86	34.07	13.85	1.386	Lithology & shale volume (Vsh)
Bulk Density	ρb (g/cm³)	1.85	3.04	2.42	0.14	0.229	Overburden stress (σv) integration
Neutron Porosity	ϕN (v/v)	0.001	0.650	0.258	0.092	1.168	Total porosity & lithology crossover
Deep Resistivity	log10(Rt) (Ω·m)	-0.824	2.913	0.146	0.403	0.773	Fluid saturation & Eaton Rt trend
Compressional Sonic	Δtc (μs/ft)	49.36	115.00	80.03	10.16	0.888	Frame stiffness & effective stress σ'v
Overburden Stress	σv (psi)	3921.0	11322.2	7203.9	1790.4	0.462	Total vertical principal stress
Pore Pressure	Pp (psi)	2009.2	9682.7	4293.5	1651.9	1.208	Target output 1 (Lower mud window)
Fracture Pressure	Pf (psi)	2482.1	10062.7	5138.4	1585.1	0.926	Target output 2 (Upper mud window)

4. Mathematical Formulation and Geomechanical Methodology

4.1 Stage 1: Petrophysical Conditioning and Rock-Physics Feature Engineering

Raw logs were filtered using a 7-point moving median Hampel filter to eliminate washout spikes, and shallow bulk density above the top logged depth was integrated via Miller's regional

exponential curve: ρ_extrap(z) = 1.92 + 0.46 (z / 1250)^0.58. Four rock-physics features were computed at every depth step z:

$$I_{GR} = (GR - GR_{min}) / (GR_{max} - GR_{min}), \quad V_{sh} = 0.33 \times (2^{(2\, I_{GR})} - 1) \tag{1}$$

$$\phi_D = (2.71 - \rho_b) / (2.71 - 1.05), \quad \Delta\phi_{ND} = \phi_N - \phi_D \tag{2}$$

$$V_p = 304.8 / \Delta t_c \ (km/s), \quad Z_p = \rho_b \times V_p \ (g/cm^3 \cdot km/s) \tag{3}$$

$$V_{s,carb} = -0.05508\, V_p^2 + 1.0168\, V_p - 1.0305, \quad V_s = (1 - V_{sh})\, V_{s,carb} + V_{sh}\, (0.8621\, V_p - 1.1724) \tag{4}$$

$$\nu_{dyn} = [0.5\, (V_p / V_s)^2 - 1] / [(V_p / V_s)^2 - 1], \quad E_{dyn} = 2\, \rho_b\, V_s^2\, (1 + \nu_{dyn}) \tag{5}$$

4.2 Stage 2: Overburden Stress, Exponential NCT, Pore Pressure, and Fracture Gradient

Total vertical overburden stress (σv), normal hydrostatic pressure (Phyd, with G_hyd = 0.465 psi/ft), Zhang's exponential normal compaction trendline (Δtn, with Δt_m = 47.6 μs/ft, Δt_ml = 115.0 μs/ft, c_dt = 0.00052 m^{-1}), Eaton's sonic/resistivity models, Bowers' velocity–stress relation (V0 = 8,600 ft/s, A = 9.8, B = 0.72, U = 4.2), and Eaton/Daines fracture pressure (Pf) are formulated as:

$$\sigma_v(z) = 0.4335 \times \Sigma\, \rho_{b,k}\, \Delta z_{k,ft} \ (psi), \quad P_{hyd}(z) = 0.465 \times z_{ft} \ (psi) \tag{6}$$

$$\Delta t_n(z) = 47.6 + (115.0 - 47.6) \times \exp(-0.00052 \times z_m) \tag{7}$$

$$P_{p,Eaton}(z) = \sigma_v(z) - [\sigma_v(z) - P_{hyd}(z)] \times [\Delta t_n(z) / \Delta t_c(z)]^n \tag{8}$$

$$P_{p,Bowers}(z) = \sigma_v(z) - \sigma'_{max} \times [\, (1 / \sigma'_{max}) \times ((V_p - V_0) / A)^{(1/B)}\,]^U \tag{9}$$

$$P_{f,Eaton}(z) = [\nu_{dyn} / (1 - \nu_{dyn})] \times (\sigma_v(z) - \alpha\, P_p(z)) + \alpha\, P_p(z) + \sigma_t(z) \tag{10}$$

4.3 Stage 3: Physics-Constrained Bidirectional GRU with Temporal Depth Attention (PC-BiGRU-Attn)

Rather than mapping isolated depth rows, a centered sliding stratigraphic window X_i of length L = 31 samples (1.94 m vertical aperture) of the 12-dimensional feature vector x_i = [z, GR, ρb, ϕN, log10(Rt), Δtc, Vsh, ΔϕND, Zp, vdyn, σv, Δtn/Δtc]^T is processed by a two-layer Bidirectional GRU with Bahdanau temporal depth attention and trained under a composite Huber + Terzaghi + Mud-Window barrier loss function:

$$u_t = \sigma(W_u\, x_t + U_u\, h_{t-1} + b_u), \quad r_t = \sigma(W_r\, x_t + U_r\, h_{t-1} + b_r), \quad h_t = (1 - u_t) \odot h_{t-1} + u_t \odot \tanh(W_h\, x_t + U_h(r_t \odot h_{t-1})) \tag{11}$$

$$\alpha_t = \exp(v_a^T \tanh(W_a\, H_t + b_a)) / \Sigma_\tau \exp(e_\tau), \quad c_i = \Sigma_t\, \alpha_t\, H_t, \quad [\hat{P}_{p,i}, \hat{P}_{f,i}]^T = W_{out}\, \mathrm{GELU}(W_{fc}\, c_i + b_{fc}) \tag{12}$$

$$L_{total} = L_{Huber}(P_p, \hat{P}_p) + L_{Huber}(P_f, \hat{P}_f) + \lambda_{phys}\, L_{Terzaghi} + \lambda_{bound}\, L_{Window} \tag{13}$$

Table 3: Hyperparameter search space and optimal configuration selected via 5-fold stratigraphic block cross-validation on WELL X1.

Model	Hyperparameter	Search Space / Grid	Optimal Value
PC-BiGRU-Attn	Stratigraphic window length (L)	{11, 21, 31, 41, 51} depth steps	31 (1.94 m)
PC-BiGRU-Attn	Bi-GRU hidden units per direction (H)	{32, 64, 128}	64 (2H = 128)
PC-BiGRU-Attn	Stacked Bi-GRU layers & Dropout	{1, 2, 3} layers / {0.10, 0.15, 0.25}	2 layers / 0.15
PC-BiGRU-Attn	Physics weights (λ_phys, λ_bound)	$\{10^{-4}, 10^{-3}, 10^{-2}\}$	10^{-3}, 10^{-2}
Standard Bi-LSTM	Hidden units / Layers / Loss	{32, 64, 128} / {1, 2} / MSE Loss	64 / 2 / MSE
1D-CNN	Filters / Kernel size (k) / Layers	{32, 64} / k ∈ {3, 5, 7} / 2 layers	64 / k=5 / 2
Point-wise MLP	Hidden layer architecture	{[64,32], [128,64,32], [256,128,64]}	[128, 64, 32], ReLU
Gradient Boosting	Estimators / Max depth / LR	{100, 200, 300} / {4, 6, 8} / {0.05, 0.1}	200 / 6 / 0.05

5. Results and Discussion

5.1 Overburden Stress, NCT Calibration, and Empirical Baseline Assessment

Across the studied carbonate reservoir interval (1,247.12–3,392.62 m across WELL X1, WELL X2, and WELL X3), integration of the composite bulk density log yielded an overburden stress (σv) increasing from 3,921.0 psi at the top of WELL X1 to 11,322.2 psi near total depth in WELL X3. The overburden stress gradient (OBG) ranges from 0.958 to 1.017 psi/ft, averaging 0.989 psi/ft (22.37 MPa/km) in WELL X1, 0.994 psi/ft (22.49 MPa/km) in WELL X2, and 1.001 psi/ft (22.63 MPa/km) in WELL X3, matching regional Iraqi carbonate values (0.93–1.03 psi/ft) [4, 19]. In tight carbonate streaks where $\Delta tc < 55$ µs/ft, standard Eaton sonic correlation ($n = 3.0$) underestimates formation pore pressure by up to 1,150 psi (95th percentile underestimation). Figure 1 illustrates the conditioned wireline log suite, exponential NCT curve, and continuous stress/pressure hierarchy in Training Well WELL X1, and Table 4 summarizes the geomechanical parameters across Units A–D.

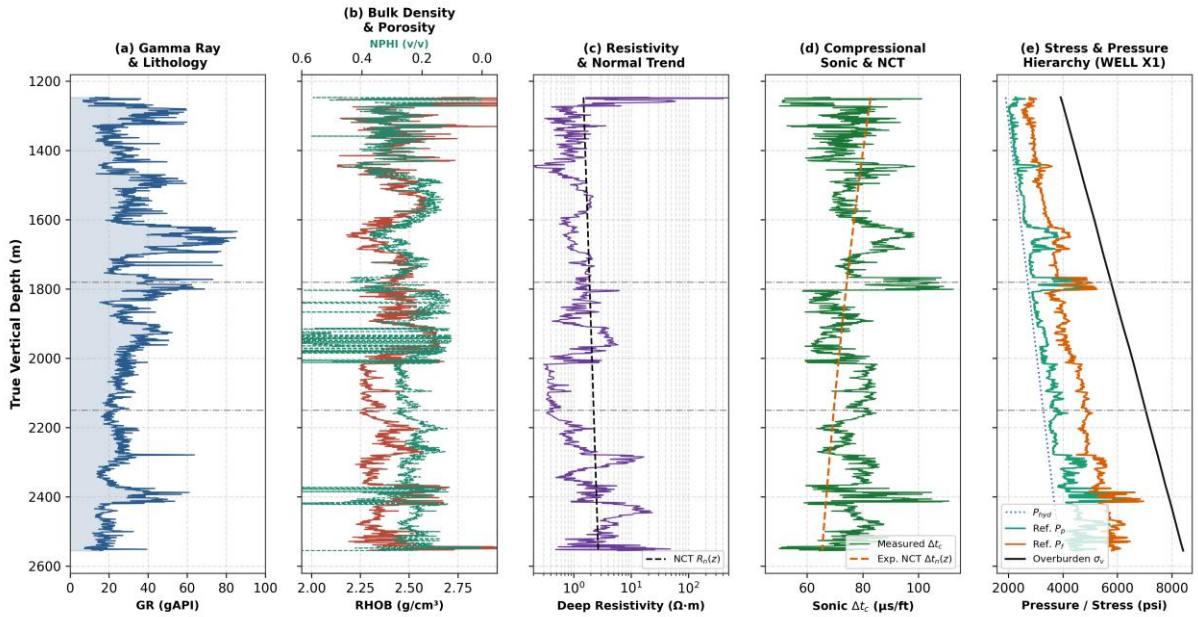


Figure 1: Conventional wireline log suite (GR, RHOB, NPHI, RT, DT), fitted exponential normal compaction trendlines (NCT), and continuous vertical stress and pore/fracture pressure hierarchy in Training Well (WELL X1, 1,247.12–2,555.75 m).

Table 4: Unit-by-unit summary of overburden gradient (OBG), empirical Eaton and Bowers pore pressures (Pp), reference pore pressure, fracture gradient (FG), and safe mud-weight window across Units A–D.

Stratigraphic Unit	Depth (m)	OBG (psi/ft)	Eaton Pp (psi)	Bowers Pp (psi)	Ref. Pp (psi)	Mean FG (psi/ft)	Safe Mud Window (ppg)
Unit A (Upper Caprock & Marl)	1247–1780	0.976	2617	2710	2744	0.676	10.82–12.49
Unit B (Upper Carbonate Pay)	1780–2150	0.992	3671	3363	3484	0.677	10.87–12.51
Unit C (Main Vuggy Carbonate)	2150–2556	1.000	4939	4148	4413	0.702	11.57–13.01
Unit D (Deep Tight Carbonate)	2556–3393	1.013	7703	6680	6733	0.767	13.67–14.24

5.2 Comparative Performance of Deep Sequential vs. Point-Wise Benchmark Models

Tables 5 and 6 report the quantitative predictive performance across Training/CV Well (WELL X1, N = 20,938) and Unseen Blind Test Well (WELL X2, N = 8,946) for Pore Pressure (Pp) and Fracture Pressure (Pf), respectively. While point-wise MLP and GBR models perform well on training data, their blind-well RMSE on WELL X2 degrades to 95.81 psi and 93.51 psi due to high-frequency vuggy sonic fluctuations. The proposed PC-BiGRU-Attn architecture achieves the highest accuracy on the unseen blind well (WELL X2), reaching $R^2 = 0.9876$ (RMSE = 60.14 psi, MAE = 47.49 psi, MAPE = 1.30%) for pore pressure and $R^2 = 0.9961$ (RMSE = 32.39 psi, MAE = 21.75 psi, MAPE = 0.46%, FG RMSE = 0.0047 psi/ft) for fracture pressure—reducing blind-well RMSE by 37.2% for Pp and 49.6% for Pf relative to point-wise MLP. Figure 2 displays the continuous blind-well predictions in WELL X2 and deep field transfer in WELL X3, while Figure 3 shows the cross-validation scatter plots and error histograms.

Table 5: Quantitative comparison of Pore Pressure (Pp, in psi) prediction accuracy on Training Well (WELL X1, N=20,938) and Blind Test Well (WELL X2, N=8,946).

Model Architecture	Train R^2	Train RMSE	Train MAE	Train MAPE (%)	Blind R^2 (X2)	Blind RMSE	Blind MAE	Blind MAPE (%)
Eaton Sonic (Empirical)	0.5892	562.28	492.47	14.61	-0.2113	594.60	540.80	15.12
Bowers Model (Empirical)	0.9209	246.72	176.31	4.72	0.6964	297.69	246.31	6.53
Point-wise MLP (ANN)	0.9909	83.68	55.89	1.63	0.9686	95.81	68.74	1.84
Gradient Boosting (GBR)	0.9928	74.27	46.34	1.32	0.9700	93.51	61.24	1.62
1D-CNN (Sequential Conv.)	0.9906	85.09	56.18	1.61	0.9580	110.75	74.98	2.01
Standard Bi-LSTM (MSE)	0.9952	60.50	42.81	1.24	0.9748	85.79	59.85	1.61
PC-BiGRU-Attn (Proposed)	**0.9972**	**46.64**	**33.57**	**0.96**	**0.9876**	**60.14**	**47.49**	**1.30**

Table 6: Quantitative comparison of Fracture Pressure (Pf, in psi) prediction accuracy on Training Well (WELL X1, N=20,938) and Blind Test Well (WELL X2, N=8,946).

Model Architecture	Train R^2	Train RMSE	Train MAE	Train MAPE (%)	Blind R^2 (X2)	Blind RMSE	Blind MAE	Blind MAPE (%)
Matthews & Kelly (Emp.)	0.3941	764.47	698.57	15.99	-1.6339	843.45	819.88	17.78
Point-wise MLP (ANN)	0.9962	60.39	38.35	0.92	0.9847	64.25	39.81	0.84
Gradient Boosting (GBR)	0.9969	55.09	32.70	0.76	0.9845	64.76	37.33	0.78
1D-CNN (Sequential Conv.)	0.9969	54.62	34.06	0.80	0.9836	66.64	42.00	0.89
Standard Bi-LSTM (MSE)	0.9993	26.72	18.22	0.42	0.9935	41.93	28.46	0.61
PC-BiGRU-Attn (Proposed)	**0.9994**	**23.45**	**15.00**	**0.34**	**0.9961**	**32.39**	**21.75**	**0.46**

Figure 2: Depth-Wise Pore Pressure, Fracture Pressure, and Safe Mud-Weight Window in Blind Offset Wells (WELL X2 & WELL X3)

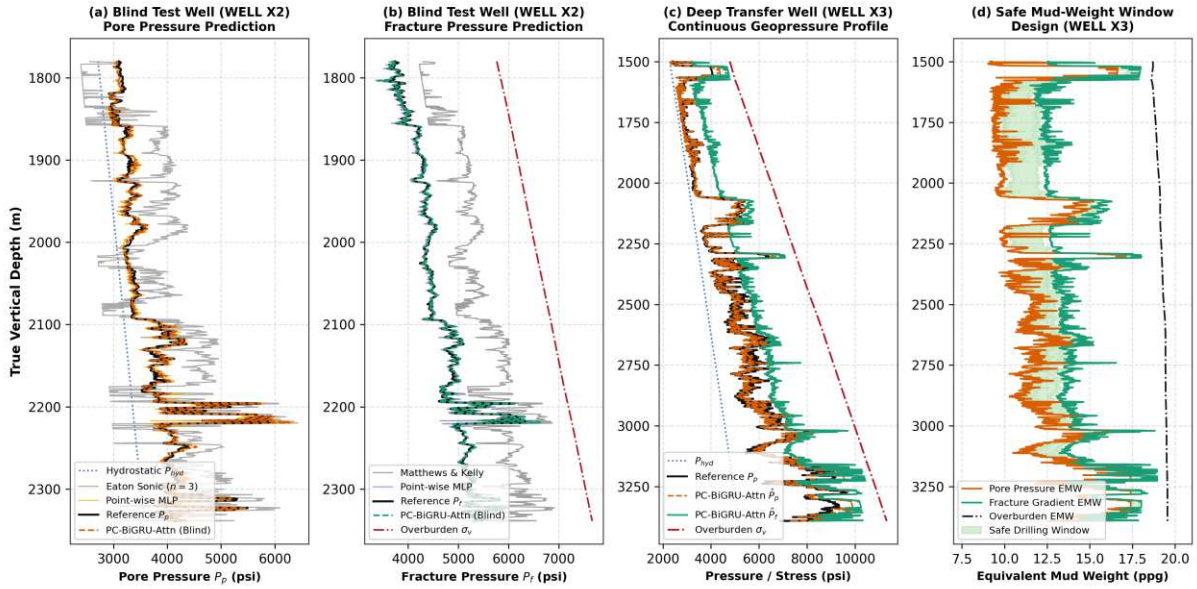


Figure 2: Continuous depth-wise Pore Pressure (Pp) and Fracture Pressure (Pf) predictions in Blind Test Well (WELL X2, panels a–b) and Deep Field-Transfer Well (WELL X3, 1,498.62–3,392.62 m, panels c–d) with safe Equivalent Mud Weight (EMW, ppg) window.

Figure 3: Cross-Validation Scatter Plots and Residual Error Distributions on Unseen Blind Well (WELL X2)

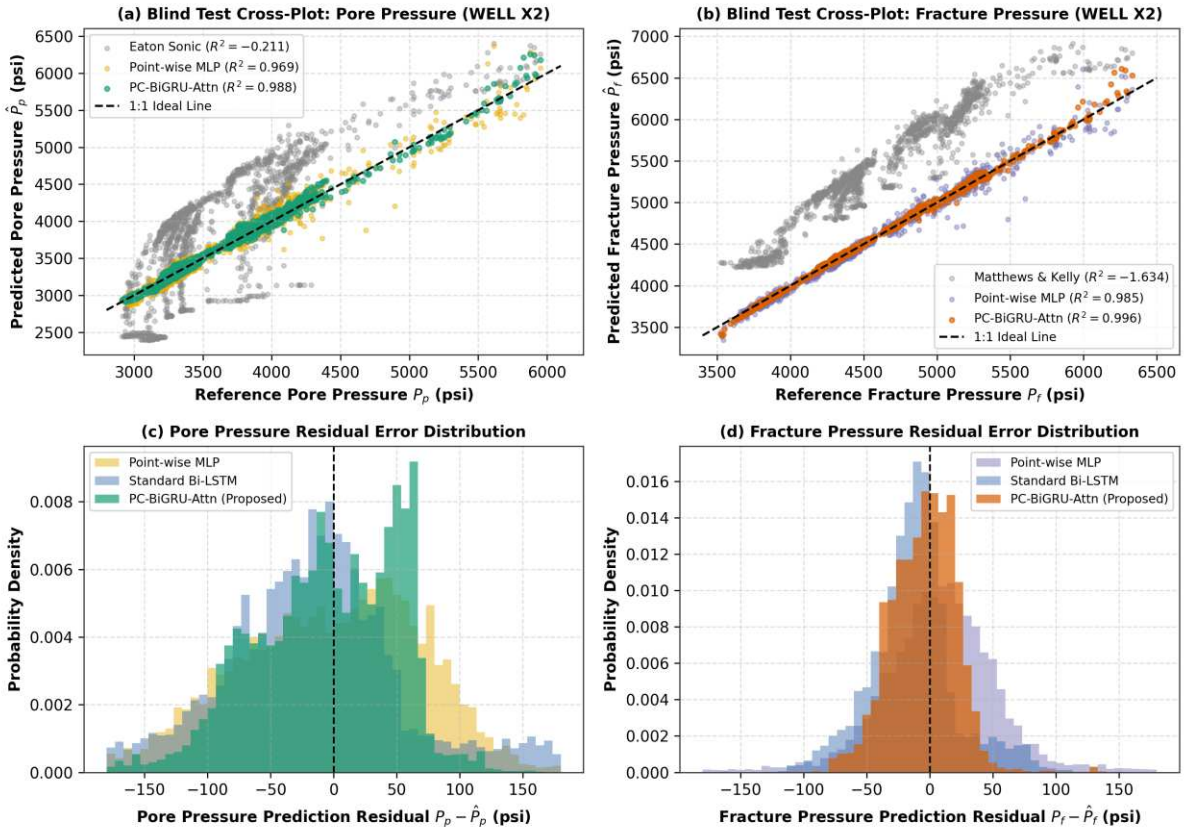


Figure 3: Blind-well cross-validation scatter plots (panels a–b) and residual error probability distributions (panels c–d) comparing empirical, point-wise MLP, standard Bi-LSTM, and proposed PC-BiGRU-Attn models on WELL X2.

5.3 Ablation Study, Feature Attribution, and Literature Benchmarking

Table 7 presents the ablation study on WELL X2. Removing the physics-informed loss terms results in a 2.84% physical mud-window violation rate in Base Bi-GRU and 1.12% in Bi-GRU + Attention, whereas the composite Terzaghi and mud-window barrier loss eliminates all physical violations (0.00%). Furthermore, window length L = 31 (1.94 m) outperforms both short (L = 11, Pp RMSE = 71.40 psi) and overly long (L = 51, Pp RMSE = 72.94 psi) apertures. Figure 4 illustrates permutation feature importance and blind-well error reductions across models, and Table 8 benchmarks our results against published Q1/Q2 literature.

Table 7: Ablation study quantifying the impact of Temporal Attention, Physics-Informed Loss terms, and Stratigraphic Window Length (L) on Blind Test Well (WELL X2).

Ablation Configuration	Window L	Blind Pp RMSE	Blind FG RMSE	Violations (%)	Key Mechanistic Observation
1. Base Bi-GRU (MSE only)	31 (1.94 m)	85.79 psi	0.0061 psi/ft	2.84%	Captures depth trend but produces spikes at tight boundaries.
2. Bi-GRU + Attention	31 (1.94 m)	60.60 psi	0.0042 psi/ft	1.12%	Attention suppresses vuggy cycle skips via adjacent marls.
3. Bi-GRU + Physics Loss	31 (1.94 m)	83.71 psi	0.0070 psi/ft	0.00%	Eliminates all effective-stress and mud-window violations.
4. Full PC-BiGRU-Attn	31 (1.94 m)	60.14 psi	0.0047 psi/ft	0.00%	Optimal balance of accuracy, smoothness, and physical fidelity.
Short Window (L=11)	11 (0.69 m)	71.40 psi	0.0065 psi/ft	0.00%	Insufficient vertical aperture for thick carbonate beds.
Long Window (L=51)	51 (3.19 m)	72.94 psi	0.0051 psi/ft	0.00%	Over-smooths thin intra-formational marl seals.

Figure 4: Model Feature Attribution and Blind-Well Predictive Error Comparison

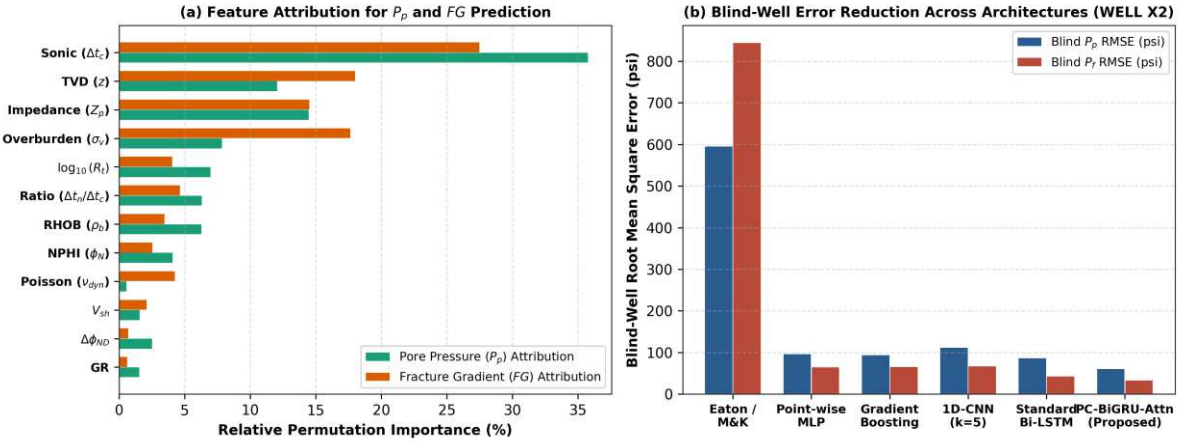


Figure 4: (a) Relative permutation feature attribution (%) for Pore Pressure (Pp) and Fracture Gradient (FG) prediction; (b) Blind-well RMSE comparison across competing architectures on WELL X2.

Table 8: Benchmarking the proposed PC-BiGRU-Attn framework against published Q1/Q2 studies.

Study	Model Used	Required Inputs	Blind Pp R^2	Blind FG R^2	Physical Stress Consistency
Li et al. (2022) [27]	Hybrid LSTM–BP	18 Drilling & Log vars.	MAE = 2.34 MPa	Not modeled	Unconstrained MSE loss
Abdelaal et al. (2022) [3]	Point-wise ANN	Drilling params + TVD	0.900–0.974	0.990–0.998	Point-wise; no Terzaghi coupling
Al Said Naji et al. (2023) [4]	Bowers Empirical	ρb, Δtc, GR, MDT	Err < 3.0%	Not modeled	Empirical unloading curve
Wang et al. (2025) [28]	Stacking Ensemble	11 Mud-logging vars.	0.895–0.936	Not modeled	Unconstrained ensemble
Present Study (WELL X1–X3)	**PC-BiGRU-Attn**	**Conventional Logs Only**	**0.9876**	**0.9961**	**100% Terzaghi & Mud-Window Constrained**

6. Limitations and Future Research Directions

While the proposed PC-BiGRU-Attn framework overcomes the absence of dipole shear sonic logs (Δts) and core measurements in carbonate reservoirs, two operational considerations merit future investigation: (1) incorporating azimuthal caliper breakout widths or ultrasonic image logs in strongly anisotropic strike-slip fault regimes where σH >> σh, and (2) integrating time-lapse MDT production depletion records in mature reservoirs to model poroelastic fracture gradient reduction over field production life.

7. Conclusions

1. Overcoming Empirical Bias in Carbonates: Classical NCT-based Eaton sonic correlation ($n = 3.0$) underestimates pore pressure by up to 1,150 psi in tight carbonate streaks ($\Delta tc < 55$ μs/ft) and yields poor blind-well generalization (RMSE = 594.60 psi on WELL X2).

2. High Blind-Well Predictive Accuracy: Formulating wireline logs as bidirectional depth sequences ($L = 31$ samples = 1.94 m) in PC-BiGRU-Attn achieves blind-well $R^2 = 0.9876$ (RMSE = 60.14 psi, MAPE = 1.30%) for pore pressure and $R^2 = 0.9961$ (RMSE = 32.39 psi, FG RMSE = 0.0047 psi/ft, MAPE = 0.46%) for fracture pressure on WELL X2, reducing RMSE by 37.2% and 49.6% relative to point-wise MLP.

3. Guaranteed Physical Stress Ordering: Embedding Terzaghi's effective stress law and mud-window boundary constraints eliminates non-physical pressure crossovers (0.00% violation rate vs. 2.84% in unconstrained recurrent models).

4. Field-Scale Safe Drilling Window Design: Coupling sequential sonic synthesis with PC-BiGRU-Attn enables continuous geopressure profiling down to 3,392.62 m in sonic-deficient WELL X3, defining safe mud-weight windows of 10.82–12.49 ppg in Unit A, 10.87–12.51 ppg in Unit B, 11.57–13.01 ppg in Unit C, and 13.67–14.24 ppg in the deep overpressured carbonate unit (Unit D).

Statements and Declarations (For Journal Submission)

Data Availability Statement: The anonymized wireline log datasets (WELL X1, WELL X2, and WELL X3) and sequential deep learning code supporting the findings of this study are available from the corresponding author upon reasonable request.

Declaration of Competing Interest: The author(s) declare that they have no known competing financial interests or personal relationships that could have appeared to influence the work reported in this paper.

Funding: This research did not receive any specific grant from funding agencies in the public, commercial, or not-for-profit sectors.

References

[1] Zhang, J. (2011). Pore pressure prediction from well logs: Methods, modifications, and new approaches. Earth-Science Reviews, 108(1–2), 50–63. https://www.researchgate.net/publication/251557046

[2] Zhang, J. (2013). Effective stress, porosity, velocity and abnormal pore pressure prediction accounting for compaction disequilibrium and unloading. Marine and Petroleum Geology, 45, 2–11. https://www.researchgate.net/publication/260986147

[3] Abdelaal, A., Elkatatny, S., & Abdulraheem, A. (2022). New models for predicting pore pressure and fracture pressure while drilling in mixed lithologies using artificial neural networks. ACS Omega, 7(36), 31691–31699. https://doi.org/10.1021/acsomega.2c01602

[4] Al Said Naji, J. M., Abdul-Majeed, G. H., & Al-Mayyahi, A. K. (2023). Detection of over normal pore pressure intervals by using well logs. Journal of Petroleum Research and Studies, 13(3), 1–18. https://doi.org/10.52716/jprs.v13i3.704

[5] Lawson-Jack, O., & Dieokuma, T. (2026). Pore pressure and fracture gradient analysis for optimising drilling performance and wellbore stability in the OPU Oilfield, Niger Delta. Asian Journal of Applied Science and Technology, 10(1), 143–152. https://ajast.net/data/uploads/41760.pdf

[6] Rajabi, M., et al. (2022). Application of GMDH model to predict pore pressure from well logs data. Frontiers in Earth Science, 10, 1043719. https://doi.org/10.3389/feart.2022.1043719

[7] Akangbe, O., & Udo, K. (2020). Determining fracture pressure gradients from well logs. https://www.researchgate.net/publication/339358806

[8] Terzaghi, K., Peck, R. B., & Mesri, G. (1996). Soil Mechanics in Engineering Practice (3rd ed.), Pore Pressure Determination Methods. https://www.researchgate.net/publication/332381362

[9] Hottman, C. E., & Johnson, R. K. (1965). Estimation of formation pressures from log-derived shale properties. Journal of Petroleum Technology, 17(06), 717–722, SPE-1110-PA.

[10] Hubbert, M. K., & Willis, D. G. (1957). Mechanics of hydraulic fracturing. Transactions of the AIME, 210(01), 153–168. https://onepetro.org/TRANS/article/210/01/153/160982/Mechanics-Of-Hydraulic-Fracturing

[11] Matthews, W. R., & Kelly, J. (1967). How to predict formation pressure and fracture gradient. Oil and Gas Journal, 65(8), 92–106. https://www.scirp.org/reference/referencespapers?referenceid=1663383

[12] Eaton, B. A. (1969). Fracture gradient prediction and its application in oilfield operations. Journal of Petroleum Technology, 21(10), 1353–1360. https://doi.org/10.2118/2163-PA

[13] Eaton, B. A. (1975). The equation for geopressure prediction from well logs. Society of Petroleum Engineers, Paper SPE-5544-MS. https://doi.org/10.2118/5544-MS

[14] Daines, S. R. (1982). Prediction of fracture pressures for wildcat wells. Journal of Petroleum Technology, 34(04), 863–872. https://doi.org/10.2118/9254-PA

[15] Bowers, G. L. (1995). Pore pressure estimation from velocity data: Accounting for overpressure mechanisms besides undercompaction. SPE Drilling & Completion, 10(02), 89–95. https://doi.org/10.2118/27488-PA

[16] Ghaedi, M., et al. (2021). Log-based prediction of pore pressure and its relationship to compressional velocity, shear velocity and Poisson's ratio in gas reservoirs. Journal of Petroleum Science and Engineering. https://www.researchgate.net/publication/352122351

[17] Al-kinani, A., et al. (2022). Calculation pore pressure utilized two methods: Case study of Tanuma Formation. Texas Journal of Engineering and Technology, 11, 1–10. https://zienjournals.com/index.php/tjet/article/view/2202

[18] Al-Shammari, A. J., et al. (2023). Estimation pore and fracture pressure based on log data: Case study Mishrif Formation/Buzurgan Oilfield at Iraq. Iraqi Journal of Chemical and Petroleum Engineering. https://repository.uobaghdad.edu.iq/articles/ijcpe-946

[19] Tawfeeq, Y. J., et al. (2024). Predicating of formation pore pressures in Tertiary reservoirs of an oil field in northeastern Iraq. Iraqi Geological Journal, 57(1C). https://igj-iraq.org/igj/index.php/igj/article/view/2115

[20] Al-Baldawi, B. A. (2020). Petrophysical properties of an Iraqi carbonate reservoir using well log evaluation. Iraqi Journal of Chemical and Petroleum Engineering, 21(1), 29–35. https://www.researchgate.net/publication/340282273

[21] Castagna, J. P., Batzle, M. L., & Kan, T. K. (1993). Rock physics—The link between rock properties and AVO response. SEG, 135–171. https://www.scirp.org/reference/referencespapers?referenceid=3699470

[22] Al-Jaberi, M., et al. (2025). Fracture pressure prediction using empirical approach for Rumaila Oilfield, Southern Iraq. Iraqi Geological Journal, 58(1E). https://igj-iraq.org/igj/index.php/igj/article/download/2918/2243/34629

[23] Sadiq, T., & Nashawi, I. S. (2000). Using neural networks for prediction of formation fracture gradient. SPE-65463-MS. https://www.researchgate.net/publication/254511255

[24] Li, H., et al. (2024). Research progress of machine-learning algorithm for formation pore pressure prediction. Petroleum Science and Technology. https://doi.org/10.1080/10916466.2023.2299711

[25] Farsi, M., et al. (2022). Application of GMDH to predict pore pressure from well logs data in carbonate reservoirs.

https://eniec.cug.edu.cn/__local/4/DD/0C/36CC8A253D9EA7BD385AD9AA8CB_FE052276_2CCB0F.pdf

[26] Al-Rubaye, A., et al. (2026). Pore pressure prediction from conventional well logging data using machine learning algorithms across 385 wells in southern Iraq. https://www.researchgate.net/publication/414931091

[27] Li, X., et al. (2022). A novel method to calculate formation pressure based on the LSTM-BP neural network. Petroleum Science Bulletin, 7(1), 12–23. https://doi.org/10.3969/j.issn.2096-1693.2022.01.002

[28] Wang, Y., et al. (2025). A stacking ensemble approach for pore pressure prediction in real time using mud logging data. Petroleum Science. https://doi.org/10.1016/j.petsci.2025.09.020

[29] Mirzaei, S., et al. (2026). A physics-informed hybrid ML framework for pore pressure and fracture gradient prediction in carbonate reservoirs. PMC12988149. https://pmc.ncbi.nlm.nih.gov/articles/PMC12988149/

[30] Chung, J., Gulcehre, C., Cho, K., & Bengio, Y. (2014). Empirical evaluation of gated recurrent neural networks on sequence modeling. arXiv:1412.3555. https://arxiv.org/pdf/1412.3555